Model-Based Verification and Validation of Component Structures for RF and Optical Experimental Systems

Charles D. Norton, Houfei Fang, Thierry Michel, Alina Moussessian, John Schiermeier, Paul Springer
Jet Propulsion Laboratory, California Institute of Technology
4800 Oak Grove Drive
Pasadena, CA 91109-8099
818-393-3920
Charles.D.Norton@jpl.nasa.gov

Richard Otero
Georgia Institute of Technology
Atlanta, Georgia 30332

Abstract— Future large aperture systems, proposed within NASA and elsewhere, will depend on integrated modeling to assess key performance parameters for designs that cannot be fully tested and verified before flight. Achieving this goal will involve integrating component and system models, results from numerical simulations, and physical tests to predict the performance and prove the viability of such systems within numerous model and measurement uncertainties. [1] [2]

JPL has built a Precision Environment Test Enclosure (PETE) and invested in development of integrated modeling software for characterizing systems relevant to radar and optical systems. We will describe the challenges and successes in how we are using the PETE and integrated modeling for thermo-mechanical and modal response of radar component structures and optical metrology testbed experiments to validate models for predictive analysis of large aperture systems.

Specifically, we will describe modeling and testing for thermo-mechanical deformation of an L-Band radar panel and our process of experimentation and parameter-based sensitivity studies performed to bring the model and measurement data into alignment. For the panel we demonstrated predictive deformations to within tenths of millimeters for the 1x1.5 meter panel for radiative heating at ~60 deg C. Radar performance analysis of a sample 50m phased-array system populated with panels of similar design will also be discussed for various observing modes. On the optical side, results from predictive modeling and physical measurements of a series of static and dynamics metrology tests on a simple reflector mounted on a composite truss in the PETE lab will be presented. Our goal, via component-based modeling, testing, uncertainty quantification, and sensitivity studies is to support predictive measurement of relative displacement of the reflector to 10s of nm as well as accurate characterization of mode frequencies and shapes. Systematic approaches to identify and quantify uncertainties in material properties and other aspects of these designs, as well as the tools used for model-based analysis, will be discussed.

Capabilities of the Cielo software, developed at JPL for integrated structural-thermal-optical modeling, will be presented along with analysis from other traditional tools such as NASTRAN, ANSYS, and FEMTools. We will conclude with the benefits of having the PETE lab for component testing compared to a high-bay environment.

TABLE OF CONTENTS

1. INTRODUCTION

In June 2007 the Precision Environment Test Enclosure (PETE) lab completed construction and acceptance testing at the Jet Propulsion Laboratory. This facility provides a unique integrated environment for deploying, characterizing and modeling large precision deployed structures. These structures will be an enabling technology for future NASA missions across the spectrum—from those in the visible to infrared, sub-millimeter, or microwave apertures too large to fit unfolded in a launch shroud. Dimensional stability is the overriding structural design driver for these large deployable apertures. The stability is driven by constraints derived from the system's mass and structural stability and to thermal and dynamical loads. As the aperture size increases, and the systems mass density is correspondingly decreased, the ability to test the performance of these apertures in a 1-g environment requires both a unique facility and special testing methodologies. The PETE is an enclosure with 10m × 5m × 3m (L × W × H) usable volume that is controlled under ambient temperature to thermal stability of

[1] 1-4244-1488-1/08/$25.00 ©2008 IEEE.
[2] IEEEAC paper #1001, Version 4, Updated July 28, 2007

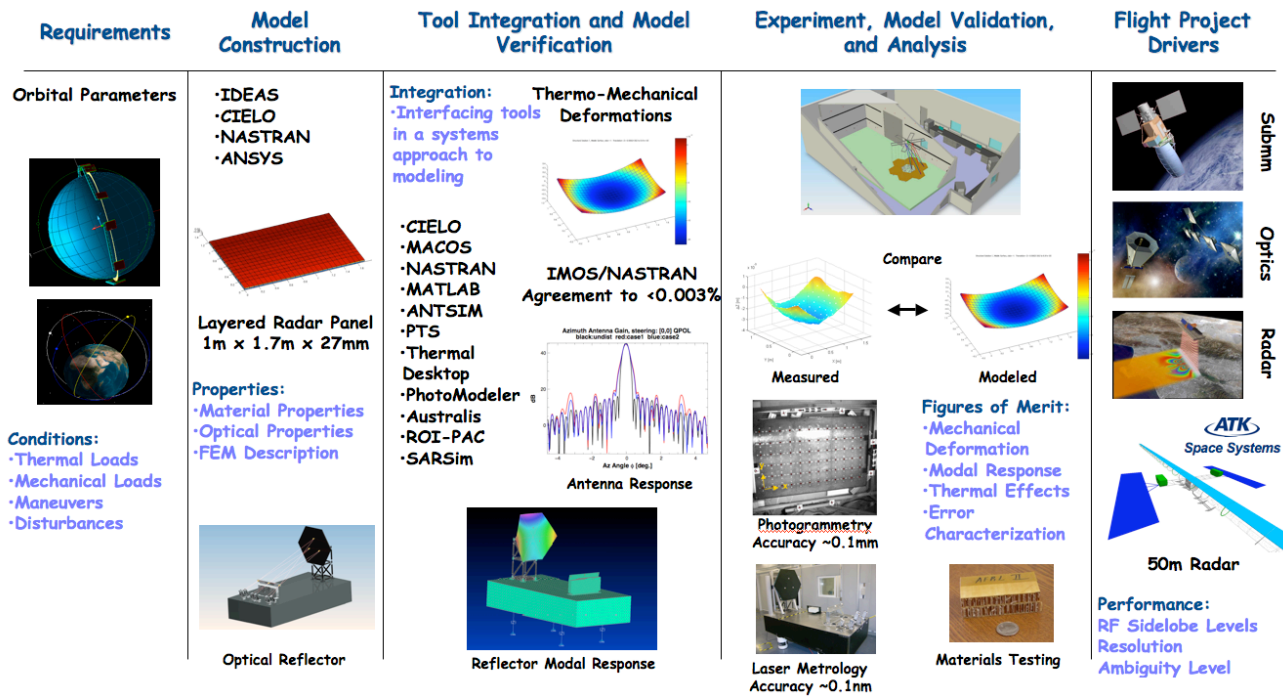

Figure 1 – Performance prediction and analysis via integrated modeling

<0.01 C°/Hr, acoustic control of <35 dBA and seismic control of <10 µgs. It has been installed within a Class 100,000 clean room and utilizes a variety of instrumentation equipment for precision measurements of structures within the room as well as the room itself [1].

Although the PETE facility can assess performance metrics of systems roughly up to 10m (longest dimension) in deployed length, a critically important part of the lab's function is to perform such analyses in collaboration with model-based analysis. These combined capabilities allow for assessment of structures that can't be physically tested via model verification and validation against components that can be characterized in this environment.

Achieving this goal requires integrated modeling and analysis for performance prediction of structures guided and impacted by quantifiable model and measurement uncertainties. Such a systems analysis flow is illustrated in Figure 1 and this represents the focus of this paper. We will describe our approach to integrated modeling and show via activities we have performed the methodology, challenges, and solutions we faced in verification and validation for RF and optical system measurements and tests.

2. Integrated Modeling and Analysis

By integrated modeling and analysis we mean the capability to assess identified performance metrics of a system by combining models, measurements, and uncertainty analysis. Our approach largely involved defining interfaces among existing tools. Although many were used, as shown in Figure 1, we placed special emphasis on a new tool in development at JPL called Cielo. Cielo supports fully integrated structural-thermal-optical analysis using a common model (realized as a finite element mesh) based on a NASTRAN hosting environment [2].

The models and measurements we will consider include:

- Thermo-mechanical deformation of an L-Band radar panel within the large aperture lab high bay.
- On-orbit performance analysis of a 50m radar antenna boom for synthetic aperture radar (SAR) operations using spotlight and quad-pol observing modes.
- Static and dynamic loading of an optical reflector kinematically mounted to a precision truss structure to measure displacement changes via a laser metrology system in air (not vacuum).

The short-term and long-term objectives of our integrated modeling and analysis include development of computer models to aid in designing physical tests and to develop initial approximations of performance; use of experimental data from tests to refine and validate computer models; use of validated computer models to assess performance of testable structures; and use of validated computer models to predict performance of non-testable structures.

3. RADAR PANEL COMPONENT ANALYSIS

At this point in the project the lab was still under construction, but most of the instrumentation equipment arrived. During this time, ATK Space Systems was also building an 8m deployable boom called SABUR – Stable Articulated Backbone for Ultralight Radar. We determined it would be useful to perform thermo-mechanical deformation experiments of the L-Band panels that could be mounted to SABUR for deployment testing. (The results of these tests, as well as aspects of material characterization would help define requirements or the "dummy" panels that would actually be used during 8m deployment testing.) Additionally, these experiments would allow us to check out our instrumentation equipment, perform initial modeling to establish test conditions and to predict panel deformation using Cielo.

Experiment Description Analysis Goals

Our goals were to predict and then validate maximal panel deformation to the mm level with a +/- uncertainty of tenths of mm. At this point, our uncertainty bounds were loosely quantified, as we had not yet measured the accuracy and precision of our instrumentation equipment and models. This included the photogrammetry system, temperature sensors, Minco heaters, influence of the support structure and suspension mechanism used to mount the panel for testing, environmental effects of the high bay as a testing area, impact of errors in the material characterization of the panel, and quality/resolution of the finite element model as an idealization of the actual panel, to name a few. For these reasons we agreed that a model uncertainty of +/- 0.4mm for maximal deformation would give acceptable agreement with the experiment.

Modeling for Experiment Design

The objective of this effort was to perform thermo-mechanical predictive modeling of the radar panel deformation using Cielo. After the tests were conducted, the measured temperatures from the panel would be assimilated into the Cielo finite element analysis. Validation of the updated results with the measured displacements would be performed, and possible sources of error in the modeling and/or test would be identified.

The radar panel we constructed measures 108.0 cm (y) by 174.2 cm (x) overall and is approximately 27.4 mm thick. It has 72 radiating patches, in a 6 by 12 array, and the patches consist of 97 mm square etched kapton/copper and measure 150 mm (y) and 130 mm (x) center-to-center. There are connectors on the surface but no transmit/receive (T/R) modules on the panels, and there are no interconnects from the ground plane to the driven patch, rendering the panel unusable for flight, but useful for our test and analysis.

The panel was modeled as homogeneous in the plane using I-DEAS, which can export a Nastran-format bulk-data file for either Nastran or Cielo. Because of the thinness of the kapton/copper, adhesive, and Astroquartz, the ground plane, driven patch, and parasitic patch were modeled as composite plate elements with "smeared" material properties. Nastran was used to smear the material properties, since Cielo does not yet have composite capabilities. (I-DEAS could also have been used, but has an error writing out the smeared properties to the bulk data file.) The honeycomb was modeled as solid elements with anisotropic material properties. The z, yz, and zx moduli have appropriate stiffness, while the x, y, and xy moduli are negligible, where the ribbon direction is in the short (y) direction. Figure 2 shows the panel layer stackup.

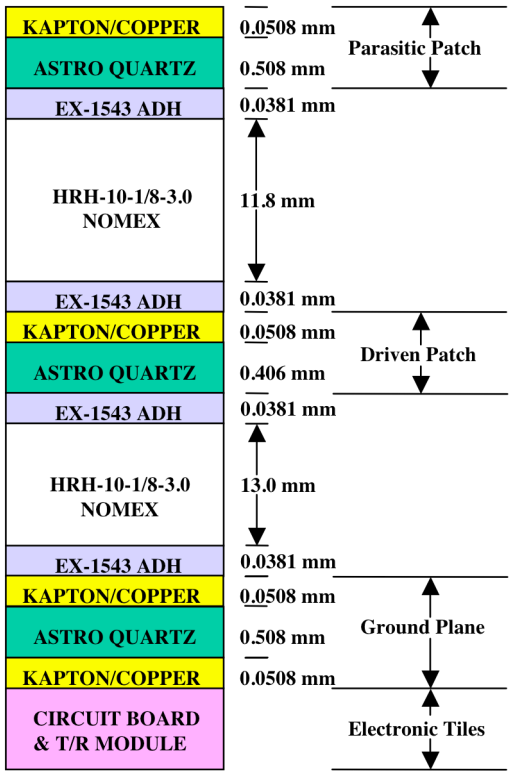

Figure 2 – Radar panel material profile

Four elements were used per patch, such that nodes coincided with the patch centers, and there were two layers of elements around the edge, such that nodes coincided with the constraint points. This yielded 1344 composite quad elements, 896 hexa elements, and 1479 nodes, for a total of 8874 degrees of freedom. Four points near the corners on the top surface were minimally constrained to represent the effects of suspending the panel, resulting in 8867 unconstrained DOF. The finite element mesh and the surface of the panel (as seen by the photogrammetry system) are shown in the Figure, 3 with elements color-coded by the element property.

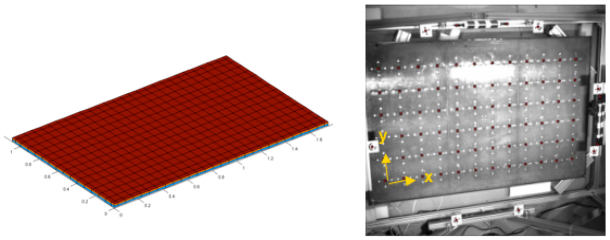

Figure 3 – FEM representation of L-Band radar panel with test article as seen by the photogrammetry system

Thermo-Mechanical Deformation Predictive Modeling

Since this is a linear analysis, any linear temperature profile can be represented as a linear combination of two load cases. The first load case assumed a 1 °C temperature

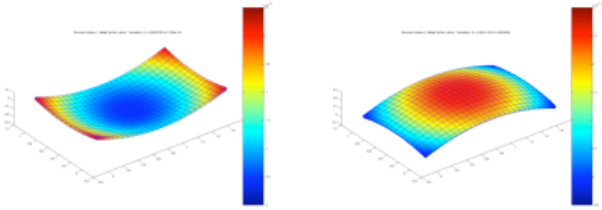

Figure 4 – FEM deformation model from Cielo analysis of temperature gradient through panel

increase on the bottom surface linearly decreasing to 0 on the top, and the second assumed the opposite condition. The panel, though close to symmetric, is not, and the two load cases will differ. They are shown respectively in the Figure 4, where the z-displacements are contoured.

The peak displacement values are -0.258 mm and 0.260 mm. These cases were also run in NX Nastran 3.0 to validate Cielo, and they exceed NX Nastran by 0.013% and 0.012%, respectively.

Performing a linear combination of the two load cases at the center of the bottom surface, approximating the results to two digits, and assuming a constant reference temperature yields the following:

$$\Delta z = -0.26\ (T_b - T_t)\ \text{mm}$$

indicating that the goal is to maximize the gradient through the thickness.

A gravity case was also run to estimate the amount of initial sag, and without non-structural mass to represent the T/R modules the maximum displacement was -0.957 mm.

Since the predictive analysis assumed constant temperature on the upper and lower surfaces, more accurate temperature data was needed. Temperatures were measured on a 3-by-5 array of resistive thermal devices (RTD's) on the lower and on the upper surfaces [3].

In order to run an improved analysis, the 30 temperatures had to be mapped to the 1479 nodes in the existing finite element mesh. Setting up a grid of temperatures and mapping each node back into the grid to linearly interpolate the temperature at that node (a pretty simplistic approach) accomplished this, but no other data was available.

Interpolations of the measured temperature data for the initial and load states are shown in Figure 5 for the bottom surface in the following figures. That for the upper surface did not vary much from room temperature, and so is not shown. The color bars are scaled to the same temperatures.

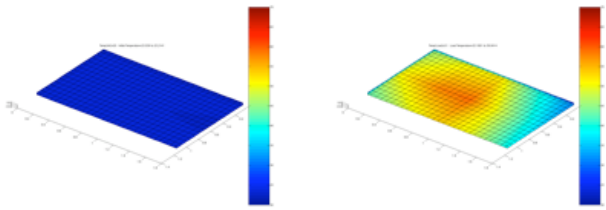

Figure 5 – Assimilation of measured temperatures into panel model for initial and loaded states

Running the thermo-mechanical model with the measured temperatures the maximum displacement was -5.11 mm as shown in Figure 6.

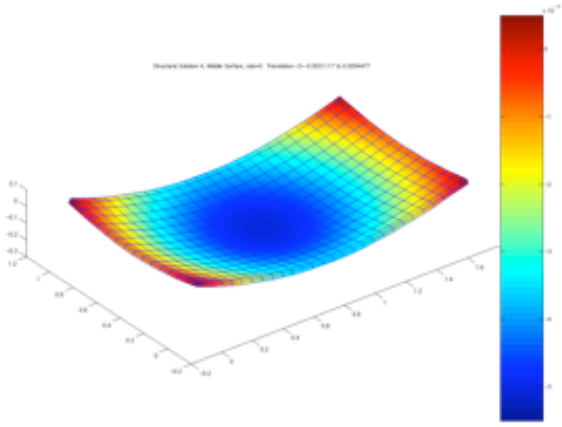

Figure 6 – Predicted panel deformation based on assimilation of initial temperature data

As will be seen from the experimental data, however, the maximum displacement in the corresponding test was -3.1 mm. Note that Nastran gave the same predictive answer as Cielo, our new analysis tool so we felt confident that the tools verified each other, but our validation against experimental data was significantly off target.

Radar Panel Deformation Experiment

Figure 7 shows the experimental setup in the high-bay of the larger aperture lab (the PETE had not yet been constructed). The panel was suspected in a manner to decouple effects of the support structure as much as possible. An analysis with the Australis photogrammetry tools helped identify

placement of the cameras to ensure 0.1 mm accurate tracking capability of targets spaced on the panel (with reference shapes for orientation). RTD temperature sensors were placed on the panel to measure the thermal load as seen by the panel compared to the applied load from the Minco heaters attached to our heat sink. The panel was heated radiatively.

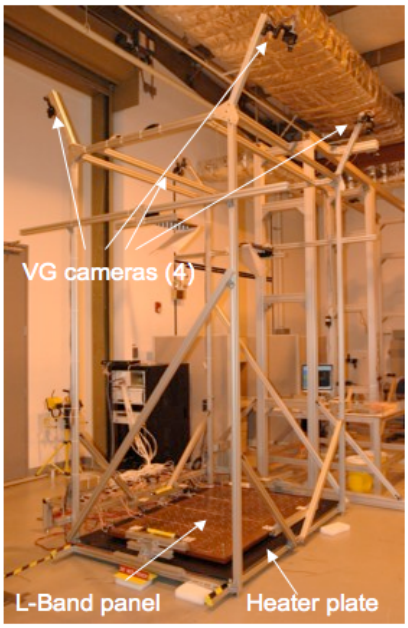

Figure 7 – Experiment setup for radar panel thermo-mechanical deformation test

The radar panel was instrumented with 114 retro-reflective videogrammetry targets (at each of 72 radar patch centers and around perimeter) and 30 resistance thermal detectors (RTDs), distributed evenly at matching locations on the top and bottom surfaces. FEM modeling was used to help design the physical testbed characteristics. A support frame was built with aluminum framing to suspend the radar panel and position the videogrammetry cameras, which needed to be 4m above the panel to capture it completely. A "heat sink" was constructed using a 5 x 5 array of Minco® Kapton heaters on a 2 x 1.3-m anodized aluminum plate. The heat sink was placed on 10 ceramic feet to provide heat insulation from the bottom of the frame. The radar panel was suspended from the support frame at its four corners, approximately 2 cm above the heat sink.

The experiment was conducted by heating the panel to a desired temperature, while taking videogrammetry and temperature measurements at several increments of time during the heating process. A videogrammetry measurement was taken by capturing a frame from each of the four cameras simultaneously using a video acquisition system. A temperature measurement was taken by simultaneously reading the temperature from all 30 RTD's, through a National Instruments data acquisition system. Videogrammetry and temperature measurements were taken within about five seconds of each other at each increment.

Before applying heat to the panel, ambient measurements were taken. A desired set point temperature was input into the heater controller, which could adjust the power supplied to the heaters through a solid-state relay, using a feedback temperature from an RTD placed on the center of the heat sink panel. To initiate the heating, 90 volts of power was supplied to the heaters by a 1000W power supply. Measurements were taken approximately every five minutes during heating. When the desired temperature was reached, the panel temperatures were monitored until they reached an equilibrium state, where a measurement was taken. If the heat sink was unable to reach the desired set point, additional power was supplied to the system, within the limits of the power supply.

Two successful runs were completed, providing equilibrium panel deformations and temperature distributions at heat sink panel temperatures of 54ºC and 62ºC. The 3D locations of the targets were obtained by processing using PhotoModeler® Pro 5 software. The deformation and temperature distribution results are as shown in Figure 8:

The maximum deflection of the panel was 3.1mm at 62ºC. The point of maximum deflection was measured to a precision of 0.1mm and was located at the approximate center of the radar panel.

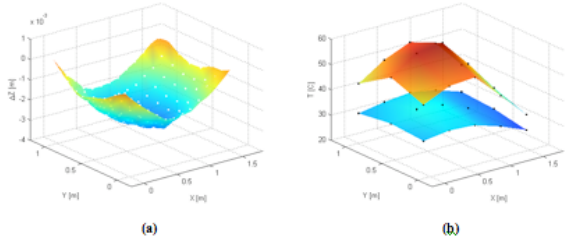

Figure 8 – Net panel deformation measurements at 62 degC (a) and top/bottom panel temperature distributions (b)

The FEM results for the displacements were particularly sensitive, in approximately a linear dependence, to the CTE of the Astroquartz, which is a combination of the fiber CTE (0.54 ppm/K), resin CTE (77.7 ppm/K), and layup of the unidirectional plies. Although we had coupons from the panel we could not measure the CTE explicitly. This led to an additional analysis to examine potential values to bring the modeled and measured displacements (-5.1 mm and -3.1 mm respectively) into better agreement.

Model/Testbed Verification and Validation

Displacements were measured on an 8-by-14 array of videogrammetry targets on the patch centers and panel edges of the upper surface only [3]. To better compare the results, the analysis data were linearly interpolated at

approximately the same measurement locations. The RMS error was determined to be 1.33 mm.

Some observations can be made. First, the constraints are more or less coincident, and there doesn't seem to be an overall translation or rotation of the panel between the analysis and test results. Second, the two result sets (and difference) have basically the same shape. This could indicate that the differences are global in nature, rather than local, such as the properties of the materials in the panel.

Sensitivity Analysis—In order to determine the sensitivity of the displacements to the material properties, several variations were run. We observed that although eliminating the thermal expansion coefficient of the honeycomb, adhesive, and kapton/copper has little effect, the max displacement varies approximately linearly with that of the Astroquartz (Figure 2). Adding offsets for the thickness of the upper and lower face sheets, as well as changing the thickness of the honeycomb layers, had little effect.

The "Astroquartz" mentioned here is actually Astroquartz II fiber in BTCy-1A cyanate ester resin that is made into a 12″ pre-impregnated unidirectional roll, of which several laminae are combined to form the laminate. The fiber has a CTE of 0.54 ppm/K, and the resin has a CTE of 77.7 ppm/K. (These values were provided by the manufacturer of the resin, Bryte Technologies; however, they did not provide values for the unidirectional sheets as sold to JPL [4].) Depending on the composition of the pre-preg and the composite layup, the material properties can vary significantly, and the value used of 12.3 ppm/K was obtained from a previous analysis [5].

Using the material properties of the fiber and resin, and assuming a mix of 60% fiber and 40% matrix by volume, ATK calculated the lamina properties, and using the layup of 45/0/-45/90/0/0/90/-45/0/45, they calculated the laminate properties [6]. This resulted in CTE's of 4.934 ppm/K and 9.007 ppm/K in the x- (long) and y- (short) directions, respectively. The resulting material moduli are also orthotropic.

The panel model was run again with the new material properties and the same measured temperatures, and the maximum displacement was now determined to be 2.78 mm. This improves upon the previous result of 5.11 mm based on the measured maximum of 3.1 mm. The RMS error was then found to be 0.28 mm, which improves upon the previous result of 1.33 mm. The difference plot (not shown here) looks like noise, rather than a global error, and the values are on the order of experimental accuracy.

Summary Comments

A predictive thermo-mechanical finite element analysis of an L-Band radar panel with uniform temperature fields was performed, using the JPL developed CIELO software. The resulting displacements, as a function of temperature gradient through the thickness, were then used to help design the test fixture and procedures.

The thermal deformation experiment was performed on the radar panel and found to have a maximum displacement of 3.1 mm, with a specified precision of 0.09 mm. Assimilating the temperatures measured from the test, the updated CIELO analysis had a maximum displacement of 2.78 mm. This corresponded to an RMS error, calculated over all the measured displacements, of 0.28 mm. However, the measured displacements of the test fixture itself in the vertical direction varied from -0.24 to 0.21 mm, which would directly affect the measured displacements of the panel.

The displacements from the analysis were then passed to the radar codes in an appropriate format (HDF5), so that they could be used to validate the performance of the panel as part of a 50m radar antenna analysis for synthetic aperture radar (SAR) applications.

4. 50M RADAR ANTENNA SYSTEM ANALYSIS

We collaborated with ATK Space to assess the performance design of a 50m radar antenna boom given deformation data from orbital maneuver conditions and geometry for wide-swath polarimetric mode (QPOL) and Spotlight (SPOT) radar observing modes (with and without metrology to capture panel and boom positions to correct for image processing). The SAR performance metrics included beam widths, side-lobe statistics, resolution, sensitivity, and ambiguities related to the design to name a few.

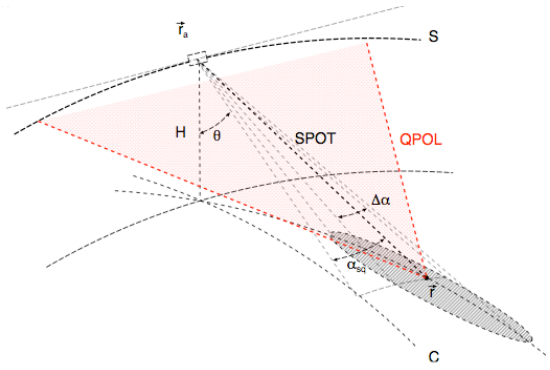

Figure 9 – SAR geometry and radar coordinates: wide-swath polarimetric (QPOL) & spotlight modes (SPOT)

A model describing the geometry of the orbit, synthetic aperture, ground swath, and antenna footprint was developed to compute additional metrics directly related to SAR performance. Figure 9 gives an idea of the footprint produced by the QPOL and SPOT modes.

Experiment Description and Analysis Goals

The performance of a spaceborne synthetic aperture radar (SAR) antenna could be adversely affected by excessive deformations in the structure supporting its radiating elements. SAR antennas are typically large to achieve sufficient gain over the swath, enhance SNR, and reduce ambiguous signals to acceptable levels. Size requirements have to be met while minimizing mass and while preserving structural rigidity to maintain performance. The deployment system, although effective, may also introduce some deformations. These considerations show the importance of

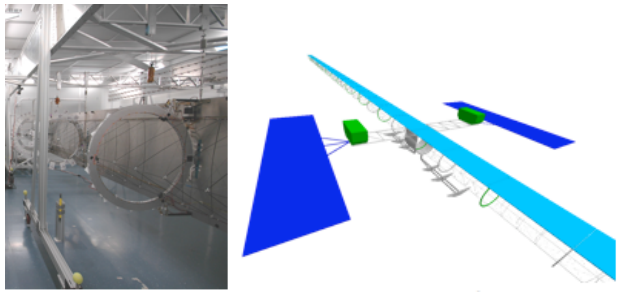

(a) (b)

Figure 10 – 8m deployable SABUR boom test article with mass-equivalent radar panels in PETE (a) with model of 50m deployed structure (ATK Space)

determining the level of performance degradations expected from typical antenna deformations in a SAR antenna assessment. Here, we discuss the implementation of a computational model that uses antenna patterns computed from a deformed antenna to estimate SAR performance parameters. The sensitivity of SAR performance to structural deformations in the antenna can thus be evaluated, and, with the addition of a deformation model, the system's performance can be simulated for realistic mechanical and thermal loads. This modeling is applied to a spaceborne L-band SAR system with an electronically steered antenna supported by a deployable structure designed and modeled by ATK as shown in Figure 10.

The antenna shape variations during the coherent dwell time can be nearly static or slowly varying when caused by thermal or gravitational effects, or by stress relief. They could also be more rapidly varying deformations, when due to vibrations or impulses such as attitude control thrusting, or due to fast attitude changes. In what follows, the rapid deformations, which are typically linear combinations of the characteristic mechanical modes of the structure, are assumed to be slower than 1/10 Hz, or with a half-period larger than the duration of the synthetic aperture. During transmit or receive, antenna deformations results in phase, amplitude, and time errors in the radiofrequency (RF) excitations of the array elements. Those errors produces distortions in the antenna gain and phase distributions. A calibration system, through which measurements of the array deformation from a metrology system are used to correct excitation errors, may be an effective system to maintain antenna performance. The impact and definition of such a system are considered here.

Traditionally, SAR antenna designers attempt to meet a set

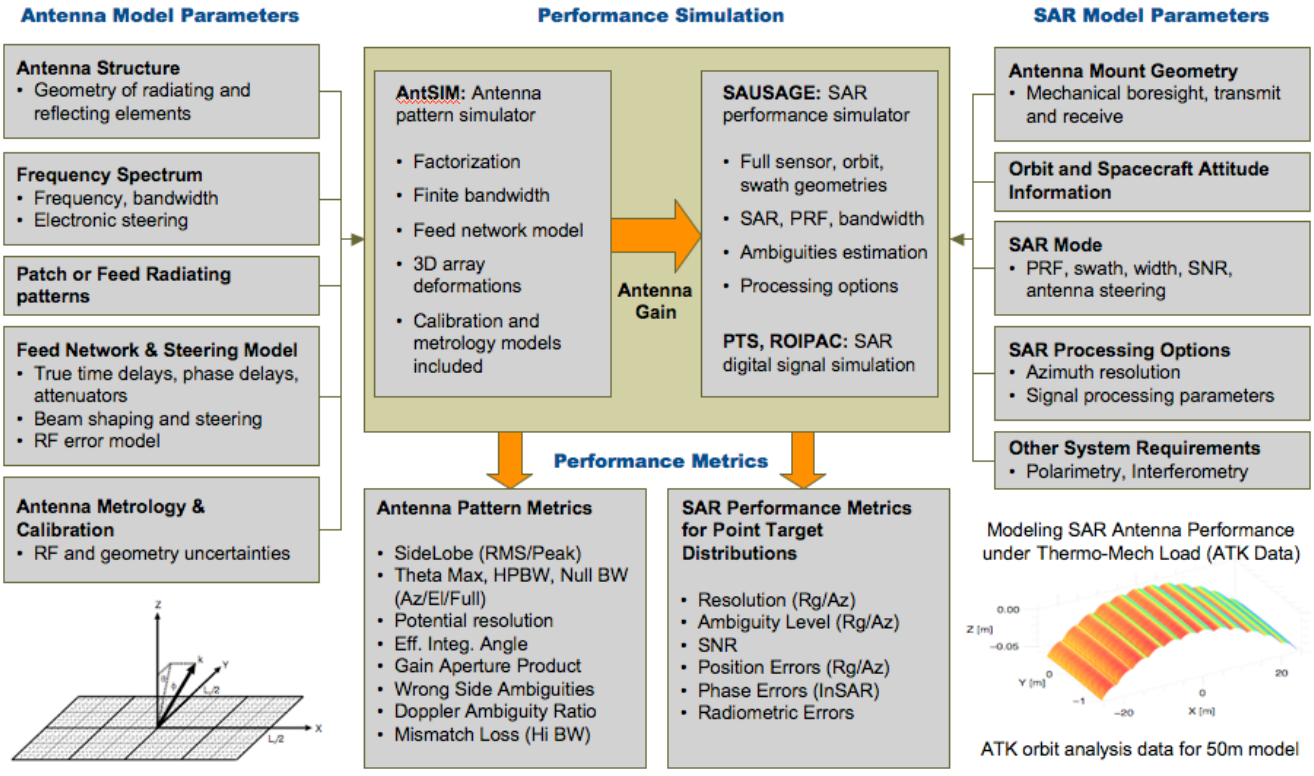

Figure 11 – Integrated radar modeling for 50m antenna SAR performance analysis

of antenna performance specifications: gain, beam-width, side-lobe levels, beam pointing accuracy, etc. These antenna measures-of-merit (MoM) are themselves derived from a set of SAR functional performance requirements, but there is no clear mapping between antenna designs trade-offs and SAR image quality. This work uses an integrated procedure in which a set of widely used SAR performance metrics can be measured directly to assess the impact of various design options and operating conditions, shown in figure 11.

Radar Integrated Modeling Development

To provide an integrated assessment approach, the distorted beam pattern obtained from a model for an electronically steered array is used directly to simulate SAR performance. The antenna pattern model is AntSim, which was originally used to support the design of a steerable phased array antenna for AFRL/JPL's Lightweight, L-band, Space-based Radar (LLSBR). In this application, AntSim provides radiation patterns used in three ways. First, the gain distributions are used to compute traditional antenna pattern metrics. Second, a sun-synchronous orbit is used, together with the prescribed spacecraft attitude and an earth ellipsoid model (WGS84), to compute the radar antenna footprint. These ground distributions of RF intensities are themselves used to compute SAR metrics that do not depend on details of each SAR mode implementation, but provide a general measure of the antenna's quality for SAR. Third, the pattern are used in a SAR analysis tool, SAUSAGE: Still Another Utility for SAR Analysis that's General and Extensible, to provide detailed performance metrics for each SAR mode.

In its general form, AntSim uses the geometry of the phased array, including its deformations, and it has a model for the network of attenuators and time or phase delays that electronically steers the array. Imperfections in the calibration of the antenna are accounted for. Metrology errors can also be introduced to determine the impact of an imperfect knowledge of array geometry if such data is used to compensate for deformations. Electromagnetic effects, such as the EM couplings between array elements or with the surrounding structure, or polarization effects, are not taken into account in the model. Although AntSim is designed to compute frequency dependent antenna gains, in this work a conventional narrow band SAR analysis is performed, and a single gain distribution at the center of frequency band is computed and applied over the entire bandwidth – this is usually a good approximation for spaceborne SARs with small relative bandwidths.

SAUSAGE is a software tool that models synthetic aperture radar and interferometric synthetic aperture radar (InSAR or IFSAR) system performance. That is, given input parameters that describe a radar system (altitude, power, bandwidth, antenna pattern from AntSim), the software produces predictions of various performance metrics (signal-to-noise ratio, resolution) for the specified system and modes.

Model Configuration, Test Cases, and Performance Effects

The combined antenna and SAR computational model is applied to estimate performance degradations with antenna deformations for an L-band spaceborne SAR in two modes of operations: polarimetric and spotlight. The antenna used is a lightweight, 1.8m × 50m phased array supported by a deployable structure designed by ATK. The array is made of 12 folding panels; themselves further divided into tiles of radiating patches with common radio-frequency (RF) feed pathways. ATK provided 6 deformation data sets typical of a low Earth (506Km), sun synchronous orbit shown in Figure 12.

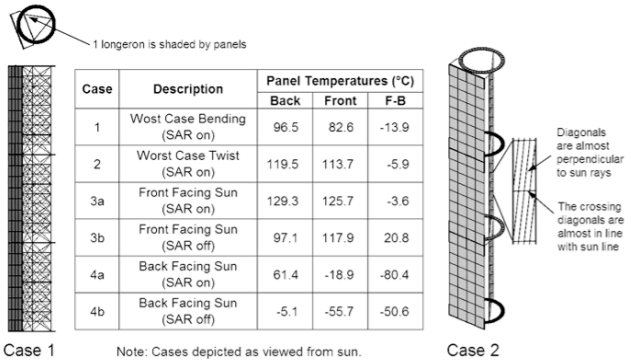

Case	Description	Panel Temperatures (°C)		
		Back	Front	F-B
1	Wost Case Bending (SAR on)	96.5	82.6	-13.9
2	Worst Case Twist (SAR on)	119.5	113.7	-5.9
3a	Front Facing Sun (SAR on)	129.3	125.7	-3.6
3b	Front Facing Sun (SAR off)	97.1	117.9	20.8
4a	Back Facing Sun (SAR on)	61.4	-18.9	-80.4
4b	Back Facing Sun (SAR off)	-5.1	-55.7	-50.6

Figure 12 – Summary of antenna load test cases

Each of the 6 files contains 3D deformation data on a quadrilateral mesh of points covering the 12 panels on the backbone. The deformation can have two main components: deformations reflecting distortions in the supporting truss, and deformation in the antenna panels themselves, mostly due to thermal effects. (Note that the panel material properties were derived from the analysis in Section 3.) The antenna geometry showing truss deflection over the 12 panels as well as deflection within each panel for these test cases is shown in Figure 13.

The three classes of SAR antenna performance figures produced by the computational model, antenna pattern, radar footprint, and SAR metrics, all show that the truss and panel deformations have different impacts on system performance. Deformations in the supporting structure exist typically over longer scales, and antenna metrics show that their main effect is to lower the peak gain and broaden the main beam, which decrease SAR sensitivity. Deformations in each of the 12 panels, on the other hand, are typically of shorter extent, and simulations show that their main effect is to increase side-lobe levels, which increases the level of ambiguous signals that are one of the noise sources in SAR. For the SAR designs considered here the latter effects are less critical than the loss in sensitivity.

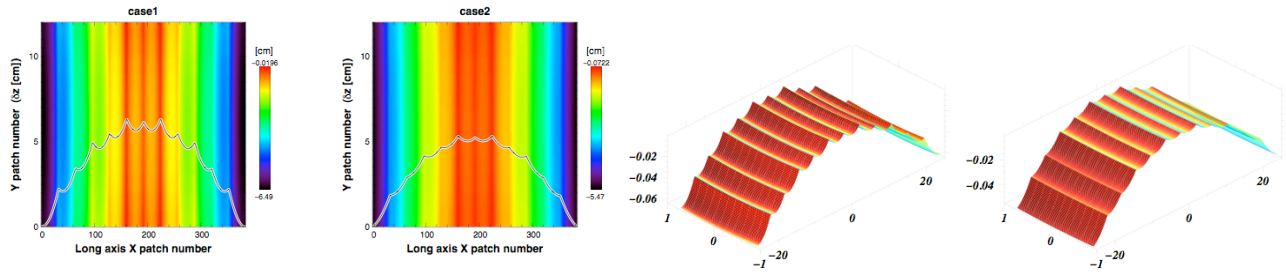

Cases 1 & 2: Z-deformation colormap (cut in X) and XYZ-deformations [m].
Convex truss deformation: peak-to-peak 6 cm. Concave panel distortion: < 1cm

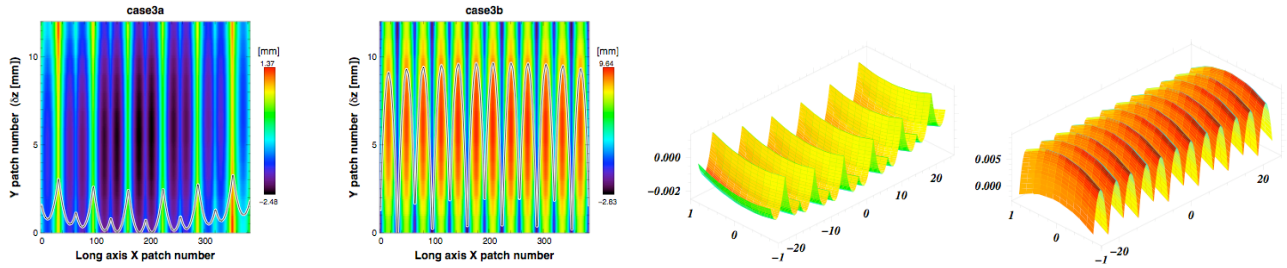

Cases 3a & 3b: Z-deformation colormap (cut in X) and XYZ-deformations [m].
No truss deformation. Panel distortions: 3a concave (3 mm), 3b convex (1cm)

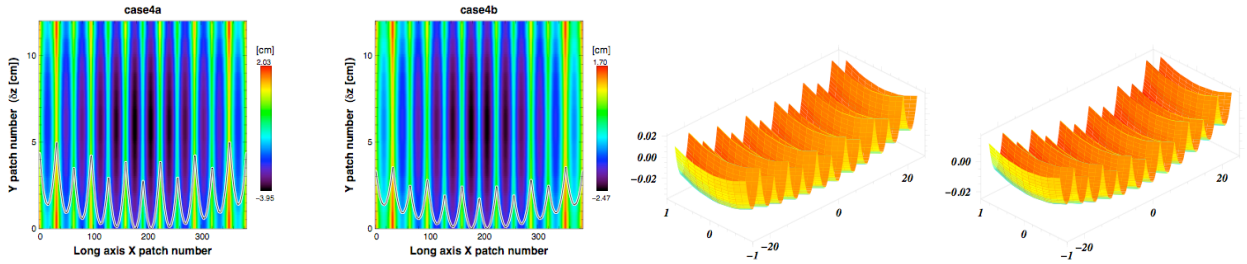

Cases 4a & 4b: Z-deformation colormap (cut in X) and XYZ-deformations [m].
Convex truss deformation: peak-to-peak 1 cm. Concave panel distortions: 4a (4cm), 4b (2cm), both roughly quadratic in X

Figure 13 – Summary of antenna geometries for load test cases

Two of the six deformation cases provided by ATK feature larger truss deflections – peak-to-peak quadratic Z deformation of about 6 cm. These worst bending and twising cases (case 1 and case 2) display roughly a quadratic bowing of the support structure supporting the 12 antenna panels. In large part, those deformations are due to the sun's thermal effect on the backbone. In addition to those, all cases also have nearly quadratic deformations of the panels, presumably due to internal (SAR) or radiative (sun) heating. In those two cases the loss of peak gain induces a radiometric error in the form of a rise in the noise floor on the order of a 1 dB, for both the wide- swath polarimetric mode and the spotlight mode. The corresponding loss in SNR is on the order of 0.5 dB (averaged across the swath.) These errors levels are commensurate to the typical total radiometric calibration error budget for surface parameter retrieval in SAR polarimetry (0.5 dB.) A metrology system enabling the calibration or compensation of these truss deformations does not need to resolve deformations at scales below the panel dimensions to restore most of the undistorted system performance.

The other four antenna shape cases have panel deformations in the Z direction that are an order of magnitude larger than truss deflections. In the four other deformation files, Case3a/b and Case4a/b, deformations localized on panels and are much larger than backbone deflections. The panel deformations themselves are of various magnitudes: from 5 mm in Case3a, where the sun's heating on the front of the panel nearly equals the SAR's heating of the back, to 5 cm in Case4a where the sun and the SAR both contribute to heating the back of the panels. Case3b is the only case with convex panel deformations in the z-direction, and is the only case with positive front-to-back panel temperature difference.

Returning to the first two cases (1 and 2) with the large truss deflection also show significant panel deformations. These panel deformations are responsible for increases in sidelobe levels, but they do not affect the shape of the main beam, or the peak gain. In all cases, panel deformations are quasi-periodic, which produce grating lobes, which are in turn responsible for increase in azimuth ambiguity levels. However the undistorted background ambiguity level is low

enough that these localized increases are not sufficient to bring the resulting average sidelobe level to critical levels.

A different SAR mode design with less tapering in the magnitude of the antenna excitations in the azimuth direction would be impacted more significantly. Grating lobes themselves may also produce partially focused "ghost" echoes that are displaced from the primary focus location, and the resulting deterministic noise level may exceed specific SAR requirements. Antenna pattern simulations show that grating lobes may be significantly reduced by means of a calibration system using metrology to accurately resolve the shape of each antenna panel.

Summary Comments

A combined antenna and SAR simulation tool is used to assess the impact of antenna deformations on system performance. Three categories of antenna performance metrics are analyzed: antenna pattern, radar footprint, and SAR performance metrics. The computational model is applied to an electronically steered array supported by a deployable structure developed by ATK. A structural deformation model of the antenna panels assembled with the truss provides data for surface displacements. Two different types of antenna deformations may be discerned in ATK's data: truss and antenna panel deformations. Case1/2 have a superposition of the two types of deformations, while the four other cases, case3a/b and case4a/b, have mostly panel deformations. The SAR metrics show that a peak-to-peak truss deformation of 6 cm is sufficient to lower the maximum gain by 0.5 dB and broaden the main antenna beam. These distortions lower the sensitivity of the SAR sensor by about 1 dB, and increase azimuth ambiguities by as much as 10 dB, in both the QPOL and SPOT modes (shown in Figure 14 for the QPOL case). The uncertainties in noise contributions to the SAR data add up to about 0.5 dB in the worse case (Case1/SPOT) and this is traditionally the total radiometric calibration budget for a polarimetric system. Given that other sources of radiometric errors are present, a compensation mechanism for antenna deformations is considered. A simple metrology model is adopted in which the antenna shape is approximated by planar facets whose positions are determined from metrology data.

Simulations show that the effect of large-scale truss deformations may be compensated using metrology and an RF calibration system that is able to correct patch excitations to account for deformations – see also [6]. Metrology measurements are assumed to be accurate enough to be able to reconstruct the shape of the radiating surface within 0.5 cm, at scales larger than the wavelength.

Deformation at a scale smaller than the size of the entire array, such as the panel deformations, are mostly responsible for sidelobe statistics – for deformations of a few cm – and do not affect the shape of the main beam.

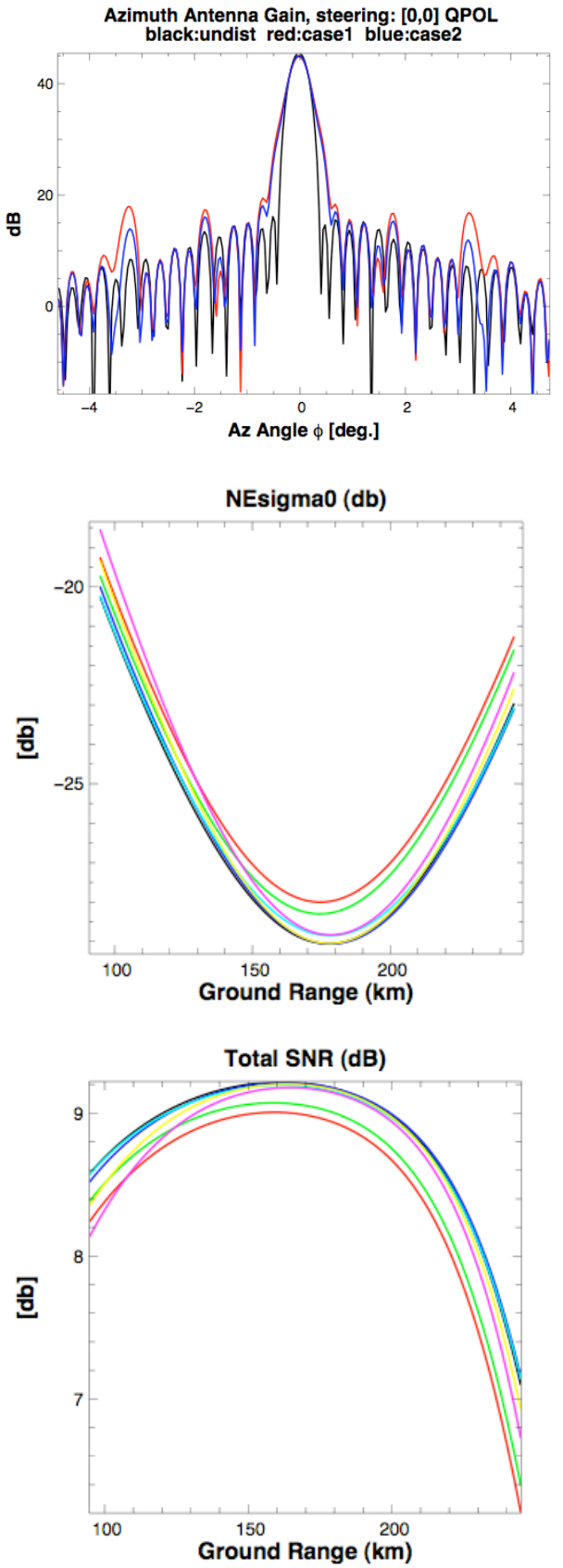

Figure 14 – QPOL Antenna pattern metrics (main beam broadening and grating lobes), and SAR performance metrics (NEsigma0 sensitivity and SNR)

When all panels show similar deformations, quasi-periodic surface displacement causes grating lobes. These sidelobes produce an increase in azimuth ambiguity levels, which is a source of multiplicative noise in SAR systems. For the specific mode designs considered here, this is a lesser issue than the sensitivity loss produced by distortions in the supporting structure.

The simulation indicates that controlling sidelobe levels by means of a calibration system requires a metrology system with a finer grid of measurements in order to be able to correctly reconstruct the shape of each antenna panel and correct for it – as expected. The major takeaway points are:

- The antenna backbone deformations broaden the main beam and reduced peak gain. Thermal distortions of the antenna panels produce grating lobes.
- The computed metrics show the impact of deformations on SAR performance.
- The most significant metric degradation is due to main-beam broadening, in part because the undistorted ambiguity levels are low, and this allows sidelobe levels to rise significantly before ambiguities can become a problem. The metrics most affected are those related to SAR sensitivity: SNR and NE σ_0.
- Overall, the SAR performance metrics for the mode considered here are not strongly affected by the expected deformations (e.g., < 0.3dB decrease in SNR and 1 dB in NE σ_0) However, if not compensated, those errors may exceed the radiometric error budget. Azimuth ambiguities due to grating lobes could become a limiter in SAR mode design.
- A calibration system using metrology to correct for antenna deformations using steering parameters should be able to restore most the lost performance as long as the metrology data describes the antenna shape correctly.

5. Optical Metrology Reflector Analysis

At this point in the project the PETE lab was complete and ready for a high precision experiment. In collaboration with the structures and metrology teams a single petal test article was designed and constructed as shown in Figure 15.

An optical truss was assembled with a kinematic mount (rod/cone/flat) to support a panel reflector. The system was mounted to a Newport table that also contained the laser beam launchers and retro-reflector. The 6 beams formed an optical hexapod via the retro-reflector and corner cubes

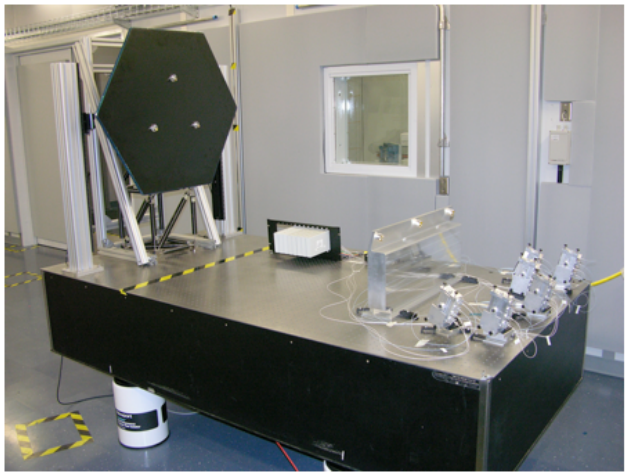

Figure 15 – Metrology single petal test article experiment within PETE lab to predict and measure beam displacements under optical truss loading

(mounted to the panel). Our objective was to perform static deformation tests while predicting and measuring displacements to micron level accuracies (absolute distances) while identifying and characterizing model and measurement uncertainties.

Experiment Description, Modeling, and Analysis

Our work started by modeling, predicting, and characterizing properties of the truss. We would then analyze the table, retro-reflector, panel, support structures leading to the construction of a full assembly model for system level modeling, analysis, and measurement.

Truss Normal Modes Analysis—We began by performing a normal modes predictive modeling of the single petal test article truss using Cielo. Validation of the results with the measured frequencies would be performed, and possible sources of error in the modeling and/or test would be identified.

The truss consists of two bays with an end structure to mount the reflector, and is constructed of thirty members. Each member consists of a graphite/epoxy cylindrical tube with two titanium end caps, which fit into the graphite tube and decrease abruptly into a thin stem with a lug. The joints are also machined titanium, and the lugs bear against bosses on the joints and are fastened with bolts and washers. Given that the nuts are torqued against the lugs, there should be negligible prestress in the tubes. The four joints at the base are fastened with screws into the optical bench. Figure 16 shows a picture of the truss.

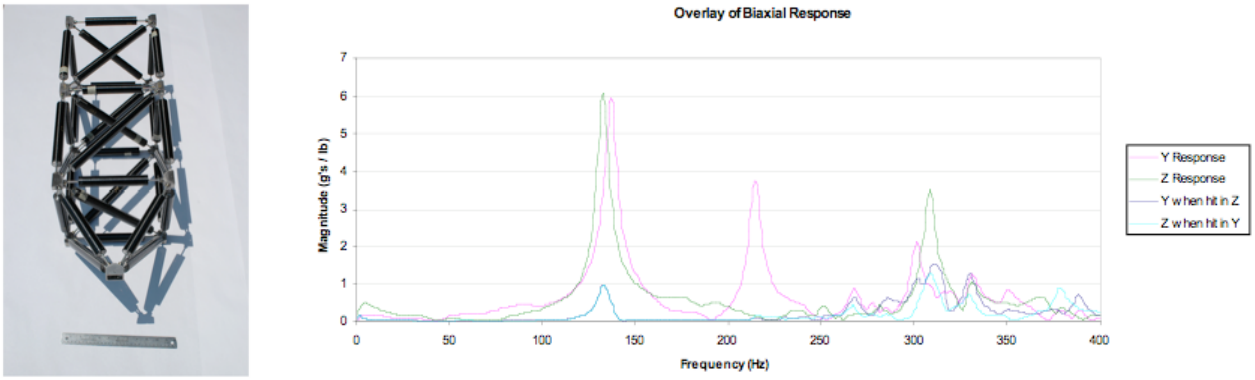

Figure 16 – Truss support with modal test response data for metrology experiment

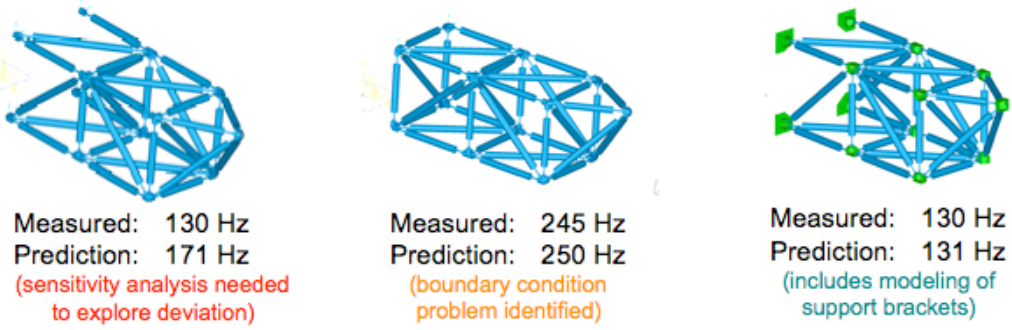

(a) (b) (c)

Figure 17 – FEM models, and variations, applied to truss to validate experiment modal measurements (1st mode)

The first three modes occur at approximately 130, 135, and 215 Hz. Given that X is the axial direction, Y is the horizontal direction, and Z is the vertical direction, it is apparent that the first two modes, green and magenta, are the vertical and horizontal bending, respectively. The smaller cyan peak near the first two modes, "Z when hit in Y", is a result of the end of the truss not being symmetric vertically. The third mode, in magenta, is most likely a torsional mode, which is excited by a Y impulse but not a Z impulse because of the non-symmetry noted above. Beyond these regions are higher-order and local modes.

The first model was a coarse model, consisting of bar elements and concentrated masses. This is a good first approximation, because forces only act upon the members at their ends. Each graphite tube consisted of one bar element for the center and one at each end, where the tube overlapped the end cap. Each end cap consisted of one bar element where the end cap underlapped the tube; one for the stem; one for the lug; and one for the joint. In addition, there were thirteen concentrated masses for the thirteen joints. Note that the joints were not modeled explicitly for the coarse model. The radius of the beam was increased and the members were rigidly attached to simulate the stiffness of the joint, and the concentrated masses were added to simulate the mass.

This resulted in 343 bar elements, 13 concentrated masses, and 253 nodes, for a total of 1506 unconstrained degrees of freedom. The graphite/epoxy was assumed to be quasi-isotropic, and each of the four bases was fixed in translation. The finite element mesh is shown in Figure 17 (a), where the bar elements are expanded to their cross sections.

A normal modes analysis was run with the base fixed, and the first three modes were 172, 176, and 246 Hz. The second mode is primarily vertical bending at 176 Hz, though there is a strong horizontal component, and that compares with the experimental value of 135 Hz. The third mode appears to be more of a local mode at 246 Hz, and that compares with the experimental value of 215 Hz. Note that the third and subsequent modes are very closely spaced. Orthogonality checks were good. The frequencies matched exactly with the Nastran results and closely with the Ansys results of 171, 176, and 237 Hz [7]. Nevertheless, these did not match the experimental results, the frequencies were significantly higher than experiment and the first two mode

Table 1 – Truss modal test and model initial results showing good model verification, but poor validation

	Test (Hz)	Ansys (Hz)	Nastran (Hz)	Cielo (Hz)
Mode 1	130	171.23	171.92	171.92
Mode 2	135	176.18	176.08	176.08
Mode 3	215	237.49	245.66	245.66

shapes were reversed.

Sensitivity Analysis—In order to determine the frequency differences, several sensitivity analyses were run. The first two varied the stiffness and masses of the joints, but the modes varied little unless the stiffness decreased or masses increased considerably. The third analysis replaced the constraints by springs and varied the stiffness, and the fourth analysis refined the tubes and the end caps with additional beam elements.

When the constraints are replaced by soft springs, the frequencies decrease significantly, indicating that the boundary conditions are suspect. When the mesh is refined, the frequencies changed very little, indicating that the mesh is adequate for the given choice of idealization (i.e. bars and concentrated masses).

Rotational constraints at the base were added, and made no difference. The optical bench was also added to the model with solid elements, but that made very little difference. In order to further test the sensitivity of the base and boundary conditions, a free/free modal test was performed. This required the addition of five tubes to the base, as shown in Figure 17 (b). Now, the lowest natural frequencies, after the six rigid-body modes, started at approximately 250 Hz and were tightly clustered and local. The lowest experimental mode was about 245 Hz, which is a much closer match.

A medium finite element mesh, each of the thirteen joints was meshed with shell elements to eliminate the concentrated masses. (Note, however, that approximate geometry was used.) This resulted in 270 bars, 90 quads, 554 trias, and 637 nodes for a total of 3596 unconstrained degrees of freedom. The finite element mesh, along with a close-up of a joint at the base, is shown in Figure 17 (c).

A normal modes analysis was run with the nodes at the locations of the bolts fully constrained, and the lowest three modes were 131, 142, and 208 Hz, which compare much more favorably with the experimental results. The first mode is the vertical bending mode of 131 Hz, which compares with the experimental value of 130 Hz. The second mode is the horizontal bending mode of 142 Hz, which compares with the experimental value of 135 Hz. The third mode is the torsional mode of 208 Hz, which compares with the experimental value of 215 Hz.

Note that unlike the coarse model, the shapes of the first and second mode correspond with the experiment, and that unlike the coarse model the third mode is clearly the torsional mode and not a local mode. The higher-order and local modes started at about 237 Hz in the numerical study.

Summary of truss normal modes analysis—A predictive normal modes analysis of the single-panel test article, using a coarse finite element model consisting of bars and concentrated masses, was performed using Cielo to develop initial approximations of performance. The resulting frequencies, which were identical to Nastran results and correlated very well with Ansys results, were then compared with the experimental results of 130, 135, and 215 Hz to validate the model.

The coarse model, with frequencies of 171, 176, and 245 Hz, showed large deviations between the predicted and measured frequencies, and so sensitivity analyses were performed on various components to determine the most

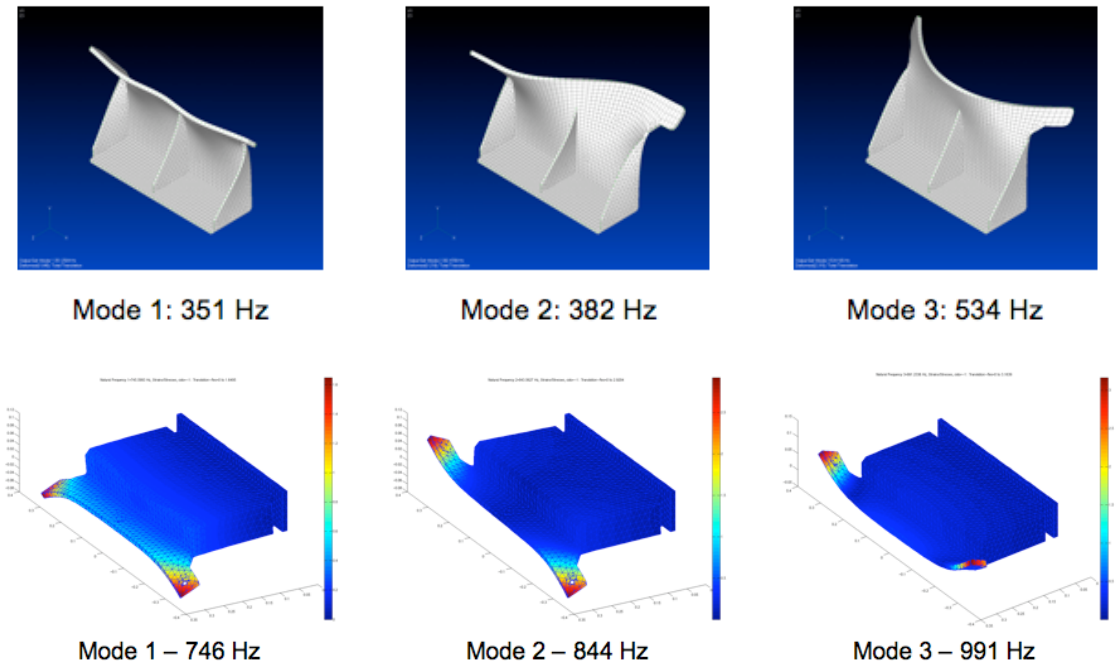

Figure 18 – Initial (top) and revised (bottom) model analysis for retro-reflector designs

critical. These were found to be the four joints at the base, where the boundary conditions were applied, and so a medium finite element model with shell elements for all the joints was constructed.

The medium model, with frequencies of 131, 142, and 208 Hz, correlated much better with the experimental results, both quantitatively in the frequencies and qualitatively in the mode shapes. This model used approximate geometry for the joints, and exact geometry would be expected to lead to even better correlation.

Retro-reflector Interference Analysis—To build an accurate assembly model of the experiment depicted in Figure 15 we needed to determine if the retro-reflector modes would interfere with the truss. The mesh for the initial design of the retro-reflector consisted of 1,680 quad4 and 877 tria3 elements, for a total of 9,738 unconstrained degrees of freedom. The Cielo results compared very favorably with the Nastran results, however, the natural frequencies were determined to be too low, and a stiffer design for the retro-reflector was desired as shown in Figure 18.

The fine mesh for the revised design of the retro-reflector consisted of 48,316 tetra elements, for a total of 228,366 unconstrained degrees of freedom; however, this was too large for the Matlab eigensolver to solve. The coarse mesh for the revised design of the retro-reflector consisted of 15,455 tetra elements, for a total of 78,756 unconstrained degrees of freedom. The Cielo results compared very favorably with the Nastran results again, and these natural frequencies were judged to be sufficiently higher than those of the truss itself so this was the final design accepted for inclusion in the assembly model.

The Assembly Model and Testing—The FEM model used in our analysis against measurement results is shown in Figure 19 along with the CAD drawing that labels retro-reflector

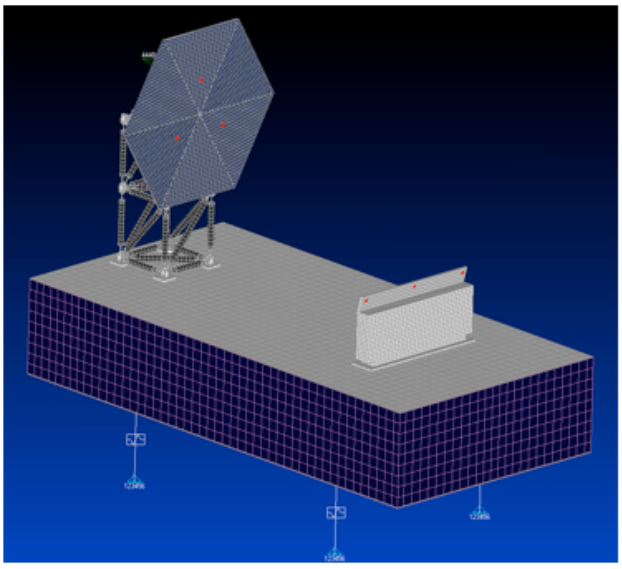

Figure 19 – FEM metrology assembly model

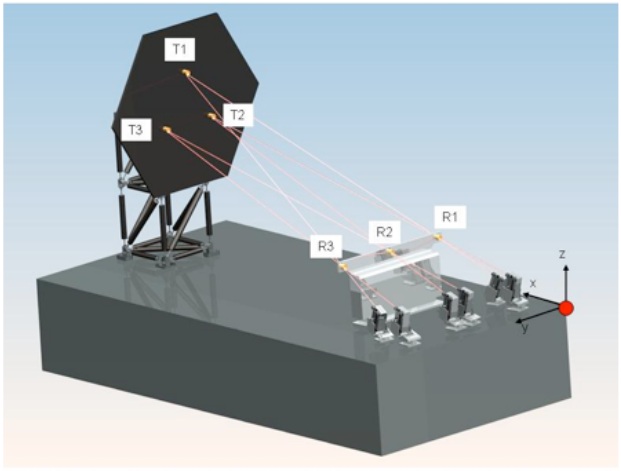

Figure 20 – Metrology CAD model

and corner cube locations used to compute displacement distances in Figure 20. The laser metrology system measured six relative displacements from the three points R1-R3 to the three points T1-T3, as shown in Figure 20, and is reported to have a 20-80 nm accuracy (in air). In general, the six beam distances form an optical hexapod and are sufficient to calculate the three translations and three rotations of the reflector panel.

The model, which included the optical table, reflector panel, and retro-reflector, consisted of 1,170 bar, 4 rod, 73 concentrated mass, 2,515 quad4, 506 tria3, 21,465 hexa, 280 penta, and 3 rigid elements, for a total of 104,677 unconstrained degrees of freedom. The relative displacements between the retro-reflector and the reflector panel were both calculated and experimentally measured. Static loads were applied to the truss only away from the metrology system, as shown in Figure 21 (exaggerated), since the reflector panel would otherwise interfere (note that the gantry used to support the stinger for dynamic testing was not included in the model, but we accounted for the contributed mass.)

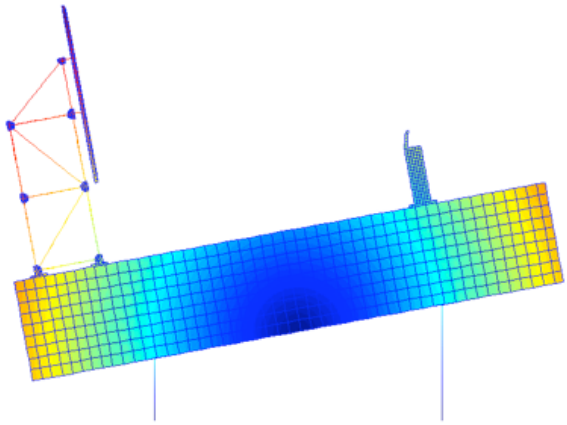

Figure 21 – System static loading on truss

Table 2 – Test measurements and model results for static loading of metrology system with 6-beam displacements

Displacements	Nastran (µm/lbf)	Cielo (µm/lbf)	Test (µm/lbf) with 1.014 lbf	Test (µm/lbf) with 1.940 lbf
R3 – T1	5.233	4.966	5.102	5.440
R3 – T3	4.139	3.932	3.879	4.145
R2 – T2	3.489	3.301	3.227	3.415
R2 – T3	4.228	4.020	4.036	4.289
R1 – T1	5.367	5.098	5.314	5.649
R1 – T2	3.572	3.381	3.323	3.538

The Cielo results agree with the Nastran results qualitatively, but are 4 to 5% lower quantitatively. Since this is consistent, it's probably due to differing element formulations.

During testing, loading and unloading of weights to pull the truss structure away from its initial position to measure displacements, we experienced non-linear behavior. The two sets of test data provide a 5 to 6% range for two different small weights with the gantry off the table. In Table 2 we note that Nastran has four relative displacements within these ranges, whereas Cielo has three within these ranges (and one barely outside). The properties of the optical table, which had to be inferred from modal and other tests since more detailed specifications were not available, are more important here because of the distance between the retro-reflector and reflector panel. Details of the magnetic latches holding the reflector panel were not modeled. Finally, all of the nonlinear concerns previously mentioned are applicable here as well.

Uncertainty Analysis—An uncertainty analysis calculated two-sigma Cielo variances for the six relative displacements, as shown in the error bars from Figure 22. These were calculated from 400 Cielo runs to generate a response surface and 138 more to verify it. The error bars for the Cielo results completely overlap the entire test range on four of the relative displacements and partially overlap on two. Pareto plots (see section 6) of the 22 error sources showed the wall thickness of the longeron carbon fiber/epoxy tubes as again having the largest effect on the uncertainty for all six relative displacements.

Summary Comments—Various components and complete assembly of the single-petal test article were analyzed and tested with the laser head and laser metrology system. The verification agreement between Cielo and Nastran results was very good. The differences were of similar direction and percent, and probably resulted from differences in the shell element formulation.

The validation agreement between test and analysis results was also good, but not as close. Several types of nonlinear behavior were observed in the tests, and these were not included in the linear analysis models. The truss members had different lengths and wall thicknesses. These were measured and could be applied individually to the analysis models. Rather than the manufacturer specifications, the

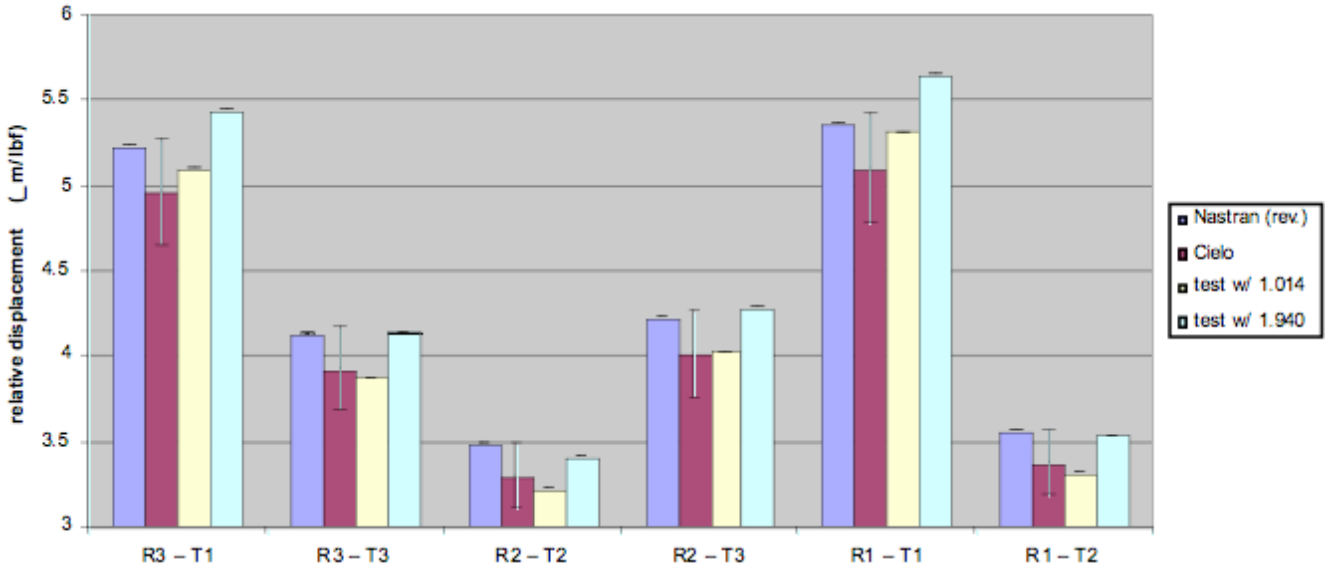

Figure 22 – Metrology experiment displacement test displacements with uncertainty analysis

moduli resulting from component testing could also be applied individually. (We did perform component stiffness tests on sample truss members and found that the modulus was lower than our nominal values. We did not however assimilate these differences into our analysis as we felt issues with the testing setup and apparatus decreased the resolution in determining stiffness values. We did not perform the tests ourselves.) Additionally, properties for some of the components, such as the optical table, were unavailable and had to be inferred from testing.

An uncertainty analysis was performed using 22 error sources to determine which had the largest effect on the uncertainties for the relative displacements. For both the laser head and the laser metrology system, the wall thickness of the longeron carbon fiber/epoxy tubes had the largest effect. Two-sigma error bars were generated for the analysis uncertainty and for the testing variation (where available). Finally, uncertainties in the finite element analyses (idealization, approximation, etc.) were not included in this uncertainty.

6. Uncertainty Quantification

We conclude this paper with a discussion of uncertainty analysis as applied to the metrology experiment just described. Observatories planned for future NASA missions will involve the reliable design of large precision deployable apertures where sensitivities to uncertainties affecting their performance must be characterized a priori. For systems that cannot be fully ground tested before flight, models that can correctly characterize the behavior of component sub-systems, to extremely small and known tolerances, must be developed. We will describe the method used to determine error bound estimates for the reflector experiment models that were produced. We performed a sensitivity analysis using a Design of Experiment (DOE) to determine uncertainty source contributions to the estimated total uncertainty present within the model.

Our efforts largely relied upon expert knowledge to perform the initial uncertainty source down-selection. A sensitivity analysis using Cielo was later performed to quantify the effects for the error sources selected. Since we felt that most of the uncertainties in our analysis could be related back to the truss structure we focused our more formal analysis on that component. Having a better understanding of the factors generating uncertainty in our response would be beneficial in:

- Serving as a guide to lowering uncertainty
- Providing guidance in the creation of error budgets
- Acting as an aid to engineering experience

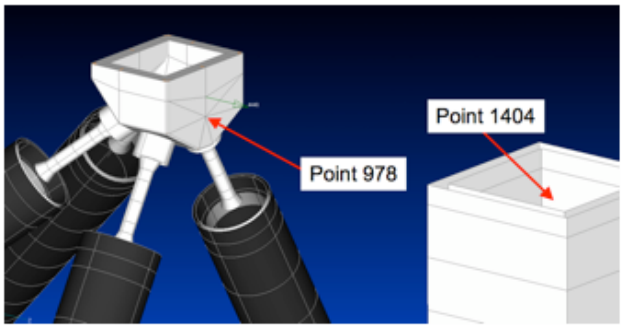

Figure 23 – Truss displacement measurement

Our study used the latest truss model available in Cielo that was verified against Nastran for tests run in the PETE. To understand truss uncertainties we used a laser displacement measurement tool in PETE testing along with the Cielo model to assess relative displacement between the truss, under loading conditions, and the laser seen in Figure 23.

The model used was composed of the truss, a model of the table and a model of the stand that would be used for the measurement laser. Changes in the relative distance between the measurement device and a point on the top joint of the truss were tracked.

Uncertainty Quantification Approach

Performing the analysis consisted of following three major steps.

1. Identifying Key Parameters—Identify input factors for testing with margins.

2. Design of Experiments (DOE)—Create DOE for input factors to generate a response surface equation. Run "goodness of fit tests" with random verification cases.

3. Applying the Approximate Model to Uncertainty Analysis—Perform Monte Carlo on the approximated model, with best current estimates for the true uncertainty sources, to easily generate an estimate of the uncertainty present in the response. A screening DOE may be performed using 2-sigma error source bounds to give a good approximation of the relative importance of each error source to the uncertainty present in the response. (If the original model or input factors change the response surface equation will have to be regenerated and verified.)

By using screening tests, one can determine ranked lists of error sources that most greatly affect the uncertainty assigned to the specified output; for the example this will be the relative displacement of the truss structure. Given a limited budget, this would provide some guidance concerning which sources of uncertainty should be concentrated on and which do not currently affect the response returned by the model. A Monte Carlo analysis will also enable the determination of one and two-sigma values that may be used as error bounds. The JMP statistical tool by SAS was extremely useful in designing the required

experiments and analyzing the data returned from the Cielo runs.

The components of the truss were separated into specific classes as identified in Figure 24. The truss model is composed of 4 separate types of beams: Battens (B), Diagonal Battens (DB), Longerons (L) and Diagonal Longerons (DL). Each beam type has a separate average length, average thickness and weight. By treating each type of beam separately, the contributions from each type can be discerned. A list of the error sources along with the testing margin in their values for analysis is shown in Table 3 (this completes step 1) used to build the response surface equation.

For step 2 a more detailed DOE was designed using the JMP statistical tool and the runs were controlled using a batch run functionality that was created for Cielo. The runs required for the DOE (roughly 400) were supplemented by 138 random cases throughout that hyperspace specified by the error source ranges. These random cases will be used for model representation error tests.

The goodness of fit tests for the response surface equation

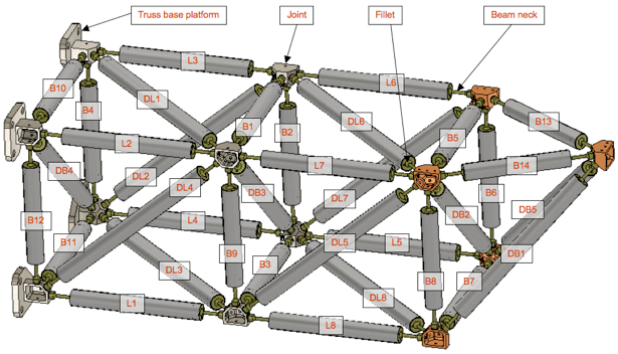

Figure 24 – Labeling of Truss Components

can be examined through a comparison between the values given by the original model and the values predicted by the RSE (see Figure 25). A tight line implies a good fit; this shows that the predicted values closely match those predicted by the approximated model. This alone is not sufficient to state that the approximation is a good fit. One must also examine the residual error compared the predicted values as shown in Figure 25. The residual is the error between the predicted value and the value returned from the

Table 3 – Experiment ranges used to construct the response surface equation

DOE Column	Error Source	Base value	Units	Range (% from base)
1	Carbon-epoxy (C-E) tube thickness, B	1.1938	mm	±30
2	C-E tube thickness, DB	1.2446	mm	±30
3	C-E tube thickness, L	1.2954	mm	±30
4	C-E tube thickness, DL	1.3208	mm	±30
5	C-E tube diameter, B	27.7368	mm	±10
6	C-E tube diameter, DB	27.7876	mm	±10
7	C-E tube diameter, L	27.94	mm	±10
8	C-E tube diameter, DL	28.0162	mm	±10
9	Titanium (Ti) neck diameter	5.08	mm	±10
10	Ti fillet approx diameter	6.35	mm	±10
11	C-E modulus, B	69	GPa	±10
12	C-E modulus, DB	69	GPa	±10
13	C-E modulus, L	69	GPa	±10
14	C-E modulus, DL	69	GPa	±10
15	Ti truss-foot platform modulus	115	GPa	±10
16	Ti end cap modulus	115	GPa	±10
17	Ti joints modulus	115	GPa	±10
18	Table top sheet modulus	190	GPa	±10
19	Table core modulus	0.418	GPa	±10
20	Table bottom sheet modulus	190	GPa	±10
21	Table leg spring constant used	1	MPa	±10
22	Force applied to truss	4.448222	N	±10

B – Battens
DB – Diagonal Battens
L – Longerons
DL – Diagonal Longerons

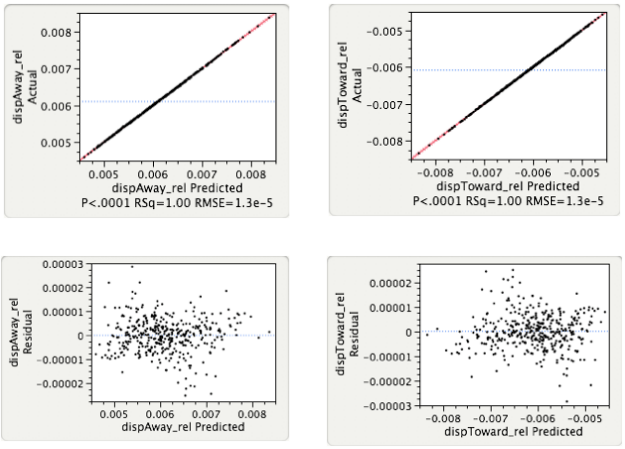

Figure 25 – Actual vs. predicted graphs for displacement tests (top) and respective residual error graphs (bottom)

original program.

We examine the residuals to ensure that the span of the residuals (here ~0.000055) is sufficiently lower than the lowest value predicted (here ~0.0045). The ratio for this example is 1.2% and is acceptable. Ratios above 5% could be a cause for concern. Also, the scatter of points in the graph should be random, similar to a shotgun blast. Patterns in the distribution of the scatter imply that there is information present within the residuals that is not being expressed in the model. Here the scatter of the residuals is not random. There is a possible third order effect that is being expressed in the residuals. One could either add several three-factor interactions into the model or conclude that the information remaining in the residuals is so small as to be easily neglected without great loss of accuracy. Since the magnitude of the residuals was small compared to the predicted response, the information remaining in the residuals was neglected.

The next test is to look at the distribution of the residuals on data that the RSE was not trained on. The extra random cases that were run enable the designer to validate the generated model.

We calculated the percent error that the residuals represent for both the training data and for the test set of random cases. For this case, 95% of the residuals are below 0.5% of

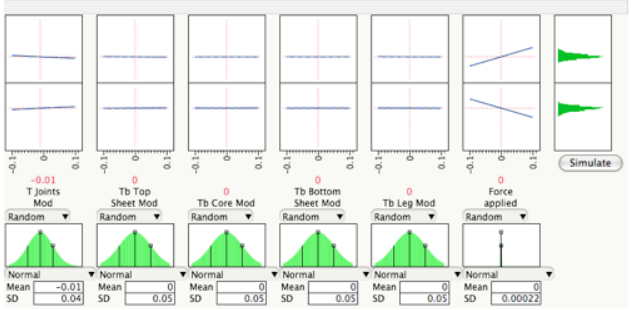

Figure 26 – Prediction profiler with distribution values for each random variable

their predicted response. The mean of the residuals is also nearly zero; suggesting that the RSE is not biased towards data that it has not yet seen. This shows an accuracy that is adequate for the uncertainty estimations

In step 3 we can run Monte Carlo simulations on our RSE as a replacement for he original model to gain fast analysis over a distribution of uncertainty input factors for a small cost in accuracy.

Figure 26 shows the setup in JMP for the prediction profiler that will be used to run the Monte Carlo. The distributions used for each of these potential error sources can be modified as new information is obtained, to reflect the change of knowledge regarding these sources of error. As the Monte Carlo is being preformed against an RSE that correctly characterizes a region enclosing the potential ranges of every error source, it can be reused each time a Monte Carlo is to be run. The overall RSE will only need to be changed when the original model itself changes and when the range for an error source extends outside of the range of the RSE.

Each line slope can be explained as the partial derivative of the response with respect to the error source being considered. Here the 'force applied' to the truss shows the greatest effect on the response over the range of ±10% error. But the actual distribution on the error source (normal distribution with a Std of 0.00022) makes it a small contributor to the uncertainty of the responses.

Impact of Error Sources—A screening DOE may be performed using the 2-sigma error source bounds to give a good approximation of the relative importance of each error source to the uncertainty present in the response. These factors can be displayed in a pareto plot where the most significant error sources are displayed at the top seen in Figure 27.

The screening analysis shows in this example that the thickness of the Carbon-Epoxy Longeron is the major source of uncertainty for both the displacement away from the laser. Though an uncertainty in the 'force applied' would cause a large increase in the uncertainty of the response, the 'force applied' has been well enough

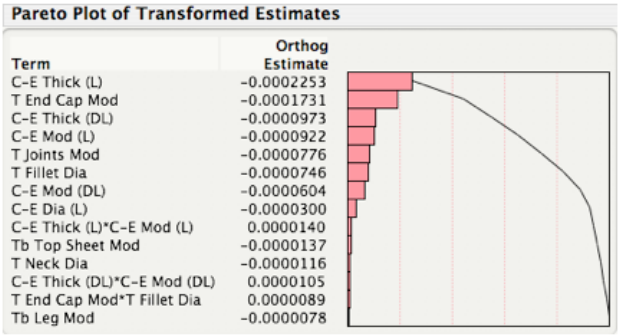

Figure 27 – Prediction profiler with distribution values for each random variable

determined that it does not appear on either list.

The Pareto chart in Figure 27 is an ordered list of the error sources that have been shown to be important in determining the uncertainty present in the response. Each red vertical line stands for 20% of the uncertainty present in the response. The black curved line represents a cumulative sum of the percentage of the uncertainty explained by the sources so far. In the example, the first 6 error sources can cumulatively explain over 80% of the uncertainty present in the response. For instance, the Pareto charts show that ~25% of the uncertainty in the responses can be explained by uncertainty in the Carbon-Epoxy thickness for the longerons.

7. CONCLUSIONS

An overview of modeling, measurements, verification, and validation associated with component test structures in our Precision Environment Test Enclosure (PETE) was presented. Radar panel thermo-mechanical deformation, analysis of a 50m antenna system for synthetic aperture radar (SAR) analysis, and static/dynamic loading of a single petal reflector system were addressed.

We have found that it is possible to characterize system performance well using a combined modeling/measurement strategy and to have component analysis impact analysis of larger systems that can't be fully tested (as shown for the 50m radar analysis). Uncertainty characterization is complex, but using tools such as JMP can help lead to a systematic analysis and design exploration of uncertainty factors and their relative impact on system analysis. The impact of having the PETE is significant as it allows for a known, quiet, environment for high precision testing as needed when laser metrology systems are used. Our future work will continue to refine our techniques further as applied to future launch opportunities where large aperture systems are needed.

8. ACKNOWLEDGEMENT

This research was carried out at the Jet Propulsion Laboratory, California Institute of Technology, under a contract with the National Aeronautics and Space Administration. It was support by the JPL Research and Technology Development Program. We also acknowledge technical support from Greg Agnes (PETE facilities lead), Keats Wilkie, Rebecca Tanimoto, Case Bradford, Feng Zhao (metrology lead), Dave Murphy (ATK Space) and Thomas Cwik (PDAS initiative leader). Finally, we acknowledge support from the Georgia Space Grant Consortium and ATK Space.

REFERENCES

[1] T. Cwik, G. Agnes, A. Moussessian, C. Norton, and F. Zhao. A Precision Deployable Aperture System Facility. 2007 IEEE Aerospace Conference, Big Sky, Montana. March, 2007.

[2] C. Hoff, M. Chainyk, G. Moore, and E. Larour. Cielo Reference Guide, JPL, 2007.

[3] R. Tanimoto, Test Report #0601. Precision Deployable Aperture Systems Radar Panel Thermal Deformation Test. Pasadena, CA. April, 2006.

[4] Bryte Technologies, E-mail to J. Schiermeier. May 2006.

[5] W. Ben Tsoi, 352D:04:03:WBT. Stress Analysis on L-band Lightweight Space Based Radar (LLSBR) Panel. January, 2004.

[6] D. McWatters, T.R. Michel, A.P. Freedman, V. Cable. Antenna autocalibration and metrology approach for the AFRL/JPL space-based radar. Radar Conference, 2004. IEEE proc., 26-29, April 2004.

[7] Z. Chang. PACTRUSS Modal Analysis. July, 2006.

[8] R. Otero. Uncertainty Quantification for Large Aperture Systems: Modeling and Test Validation. JPL, August, 2007.

BIOGRAPHY

Charles D. Norton is a Principal Member of Technical Staff at the Jet Propulsion Laboratory, California Institute of Technology and Supervisor of the Model-Based Systems Engineering and Architectures Group. He received his Ph.D in Computer Science from Rensselaer and his B.S.E in Electrical Engineering and Computer Science from Princeton University. Prior to joining JPL he was a National Research Council resident scientist. His work covers advanced scientific software for Earth and space science modeling with an emphasis on high performance computing and finite element adaptive methods. Additionally he is leading efforts in model-based validation of precision deployable structures and development of smart payload instrument concepts. He has given 32 national and international keynote/invited talks; published in numerous journals, conference proceedings, & book chapters. He is a member of the editorial board of the journal Scientific Programming, the IEEE Technical Committee on Scalable Computing, a Senior Member of

IEEE, recipient of the JPL Lew Allen Award, and a NASA Exceptional Service Medal.

Houfei Fang *is a consultant in software development methodology and technology. He has developed and led development of software at Bell Labs, RAND, Scientific Data Systems, Xerox, Honeywell, and Groupe Bull. He previously served as Director of Honeywell and Groupe Bull's Los Angeles Development Center, where the operating systems, databases, compilers, and communications software for the CP-6 system on main-frame hardware were developed and supported. He has held management positions at startups International Meta Systems in 1987 and Acorn Technologies in 1997. In the early 1960s he wrote the operating system for JOSS II, one of the earliest timesharing systems. He has a BSEE from Caltech and a master's certificate in communications from Bell Laboratories.*

Thierry Michel received the Ph.D. degree in physics in 1990 from the University of California Irvine. At the Jet Propulsion Laboratory, Pasadena, he has worked on digital processing and applications of airborne and spaceborne SAR. This has included theoretical modeling of scattering from the ocean and in forest canopies , and retrieval algorithm development for geophysical parameters using SAR interferometry. He has also participated in the development of processing and calibration systems for JPL/NASA across-track interferometers: TOPSAR, IFSAR, GeoSAR, and UAVSAR.

Alina **Moussessian** received her Ph.D. in Electrical Engineering from Caltech in 1997. At Caltech she worked on microwave and millimeter-wave power combining, beam-steering, computer-aided design and microwave circuits. After graduation she joined the Radar Science and Engineering Section at JPL where she worked on Shuttle Radar Topography Mission (SRTM) radar testing and the development of a testbed airborne radar sounder for the Europa Orbiter Radar Sounder. She worked in industry from 2000 to 2001, developing optical telecommunication components. Since returning to JPL in 2002 she has been involved in technology development projects for very large aperture phased arrays. She is currently working on membrane radar systems for future NASA missions and advanced components technology for membrane-based phased arrays. She is currently the supervisor of the Radar Technology & Hardware Implementation Group.

John Schiermeier earned his Doctor of Science at Washington University in St. Louis in 1990, specializing in the p-version of the finite element method. He worked for Noetic Technologies in St. Louis for six years, developing the p-version code Probe, and for the MacNeal-Schwendler Corporation in Los Angeles for 11 years, developing Nastran. Since then, he has worked for five years at JPL developing and applying the coupled thermal-structural-optical analysis code Cielo.

Paul Springer is a member of the technical staff at the Jet Propulsion Laboratory. He received a BS degree in mathematics from Wheaton College, and his Master's degree in mathematics from Caltech, and has been working at JPL since that time, with the exception of 7 years when he was involved in database work at Ashton-Tate. His responsibilities at Ashton-Tate included being technical project manager for dBASE III and dBASE Mac, both commercial database products. During that time he also wrote a database related book which was published in 1988. In 1990 he left Ashton-Tate to return to JPL and became involved in parallel and distributed computing, a field he has worked in since that time. He specializes in simulation work, particularly in parallel discrete event simulation. Recent tasks have included building simulations of networks as well parallel system architectures for a future generation petaflops-capable computer, funded by DARPA's HPCS program.

Richard E. Otero is an Aerospace Engineering Ph.D candidate at the Georgia Institute of Technology where he is also pursuing a M.S. in Computer Science specializing in intelligent systems. He received his B.S. in Computer Science from SUNY New Paltz. Currently he is the design and development lead for the Planetary Entry System Synthesis Tool (PESST) under development at the Space Systems Design Lab (SSDL) at Georgia Tech. During his time at JPL, Richard worked on statistical methods to quantify uncertainty sources present in the modeling of deformations for large aperture optical systems. He is a Sloan Foundation Graduate Scholar and a GEM fellow.